Vortex-induced vibration of a piggyback pipeline half buried in the seabed

Dixia Fan [a,*], Baiheng Wu [a,b], Divya Bachina [c], Michael S. Triantafyllou [a]

[a] Massachusetts Institute of Technology, Cambridge, MA 02139, USA
[b] Norwegian University of Science and Technology (NTNU), Trondheim, 7491, Norway
[c] Boston University Academy, Boston, MA 02215, USA

ARTICLE INFO

ABSTRACT

Experiments were conducted in a tow tank on the steady current-induced vibration of the smaller flexible cylinder (aspect ratio $L/d = 61$ and mass ratio $m_0 = 1.38$) in a piggyback configuration with the main pipe half-buried in the seabed. The effect of the gap-to-diameter ratio (G/d) based on the smaller cylinder diameter is studied for five different configurations from 1.0 to 4.0 and ∞ (open flow) at different reduced velocities (Ur) from 2 to 10 based on the 1st modal natural frequency. An underwater optical measurement system was used in the current experiment to acquire both cross-flow (CF) and in-line (IL) vibration with a both spatially and temporally dense format. The results show that the existence of the half-buried larger cylinder will increase the mean drag coefficient for the smaller flexible cylinder and induce a positive mean lift coefficient pushing it away from the larger cylinder. For the smallest gap-to-diameter ratio of $G/d = 1.0$ when the interaction is the strongest, experiments show that the root mean square (RMS) of the CF vibration will increase due to the appearance of the stronger higher harmonic motion compared to the open flow case. The results of the inversely calculated vortex forces reveal that the 3rd harmonic fluid force in the CF direction is even stronger than the 1st harmonic fluid force for $G/d = 1.0$. In addition, it is found that there is a strong correlation between the positive lift coefficient in phase with velocity (C_{lv}) and the counter-clockwise trajectory between the CF and the IL vibrations of the smaller flexible cylinder, even with the existence of the large half-buried main pipeline.

© 2019 Elsevier Ltd. All rights reserved.

1. Introduction

In the offshore industry, marine pipelines are widely used for oil and gas transportation. Due to economic and technological reasons, there has been a rise in the use of multiple pipelines coming as a bundle. One of the many setups consists of two parallel circular cylinders with different diameters, commonly referred to as the "piggyback" configuration. The larger pipeline is used for transporting oil and gas, while the secondary pipeline serves as an addendum for hydraulic fluid control or signal transmission. In the field, the primary pipeline will usually be directly put close to or even half-buried on the seabed, while the smaller one is installed directly above at a certain distance. When facing current, the problem of vortex-induced vibration (VIV) [1] may arise and has to be taken into serious consideration as it may decrease the structural fatigue life [2].

Due to the significance of VIV to both engineering application and scientific research, a vast number of studies in the past few decades have been dedicated to understanding the hydrodynamic force [3] and vortex formation [4] of a uniform rigid cylinder

---

* Corresponding author.
  E-mail addresses: dfan@mit.edu (D. Fan), baihengw@stud.ntnu.no (B. Wu), bachina@bu.edu (D. Bachina), mistetri@mit.edu (M.S. Triantafyllou).

placed in a uniform current undergoing VIV. In addition, a small change of the cylinder configuration will drastically alter the VIV nature of the system. Two common variations are flow-induced vibration of two cylinders in side-by-side configuration [5] and steady flow past a horizontal cylinder near a plane [6]. Numerous results have revealed that the existence of the second cylinder would alter the vibration amplitude, vortex shedding, and synchronization of the two cylinders based on their relative locations [7], while the plane boundary was found to help to suppress the vortex shedding as well as VIV when the spacing is small between the wall and cylinder [8].

As described above, piggyback pipelines are one unique configuration of two cylinders with different diameters bundled together, and they are usually placed directly near or in the seabed. Therefore, it combines the above two configuration variations as the multiple cylinders close to a plane. Because of its complicated configuration, there are much less research on the topic. Kalghatgi et al. [9] first experimentally investigated and determined hydrodynamic coefficient C_d and C_l of a static piggyback pipeline bundle with a certain proximity to the seabed and found that the hydrodynamic coefficients were strongly correlated to the gap between the seabed and the main pipe. Using a hydro-elastic facility in a conventional water tunnel, Zang et al. [10] experimentally modeled and investigated the VIV and vortex shedding [11] of a near-bed piggyback pipeline bundle with different configurations. They investigated the effects of the diameter and gap ratio between the two cylinders and the spacing between the seabed and the main pipeline, as well as the position angle of the smaller cylinder towards the bigger one. They found that with the presence of the secondary cylinder and bottom plane, VIV can be effectively suppressed as the maximum peak amplitude decreased by 25%. Furthermore, they measured the flow field around a static piggyback pipeline near a plane and explained the vortex shedding suppression and hence the VIV suppression mechanism via vortex swirling strength analysis [12]. In addition, there were also a few numerical simulations by Zhao et al. [13], which quantified vortex shedding modes for the near-seabed piggyback pipeline as a function of the gap, spacing ratios and the position angles of the smaller cylinder [14].

However, the complexity of the problem does not just stop here for the configuration variation of the rigid cylinder VIV, as when the cylinder aspect ratio becomes larger, the system becomes flexible and hence the rigid model is no longer sufficient [15]. As mentioned before, the existing studies on the hydrodynamics and VIV of the piggyback pipelines focus on the response of the two rigid cylinders together as a bundle. Meanwhile, the secondary pipeline itself, when open to a running current, may experience oscillation as a flexible cylinder, due to its large aspect ratio ($L/D > 50$). However, until now, there has been no study on the VIV response of the smaller flexible cylinder in the piggyback configuration with an influence from the primary pipeline half buried in the seabed.

Hence, in the current study, VIV of a smaller flexible cylinder close to a larger D-shaped cylinder on a plane boundary was physically modeled and studied in a towing facility. A series of experiments have been conducted to understand the effect of the different gap-to-diameter ratios on the flexible cylinder VIV response of the secondary pipeline half buried in the seabed.

2. Experiment description

2.1. Model and experimental setup

Current experiments were performed at MIT Tow Tank with a towing length of 30.48 m and width of 2.44 m, and the water depth was kept as 0.9 m. An aluminum frame was built to provide stiff mounting points for the model to the carriage. The model was clamped on both ends and chosen to be installed and tested vertically with a total 98% immersed length, and hence there is no initial sagging issue compared to a horizontally installed model. A 6-axis ATI Gamma sensor was installed on the top, measuring forces applied on the model top in each experiment run. A flat aluminum board was constructed with a D-sectioned cylinder installed as the larger pipeline half buried in the seabed. The total configuration is sketched in Fig. 1.

The diameter of the main pipeline model was chosen to be $D = 2.54$ cm ($1 in$), that of the smaller flexible cylinder was chosen to be $d = \frac{3}{8}D$ and the length was picked as $L = 58.1$ cm, keeping an aspect ratio of 61 for the smaller cylinder. In this paper, we follow the convention that the top model is set to be $L/d = 0$ and the bottom of the model is set to be $L/d = -61$. The flexible model was constructed/molded via urethane rubber with a mass ratio of 1.38 (structural mass to displaced fluid mass). In addition, a fishing line was embedded in the model center, providing sufficient axial strength while keeping a very low bending stiffness. Compared to the applied tensions in the current experiment, the bending stiffness of the urethane rubber model was measured to have a negligible contribution to the model's natural frequency and modal shape, and hence the model displayed a string-like vibration behavior. The detailed parameters of the model are listed in Table 1.

Five different gap-to-diameter ratios were chosen in the current experiment, and eight different velocities from 0.15 m/s to 0.50 m/s were performed, resulting in a Reynolds number ranging from 1400 to 4,800, based upon the diameter of the flexible model.

2.2. Optical measurement technique

In the current experiments, underwater optical methods were applied to capture the CF and the IL vibrations at a total of 20 points (staggered black and white markers) along the model. Compared to the traditional strain-gauge and accelerometer
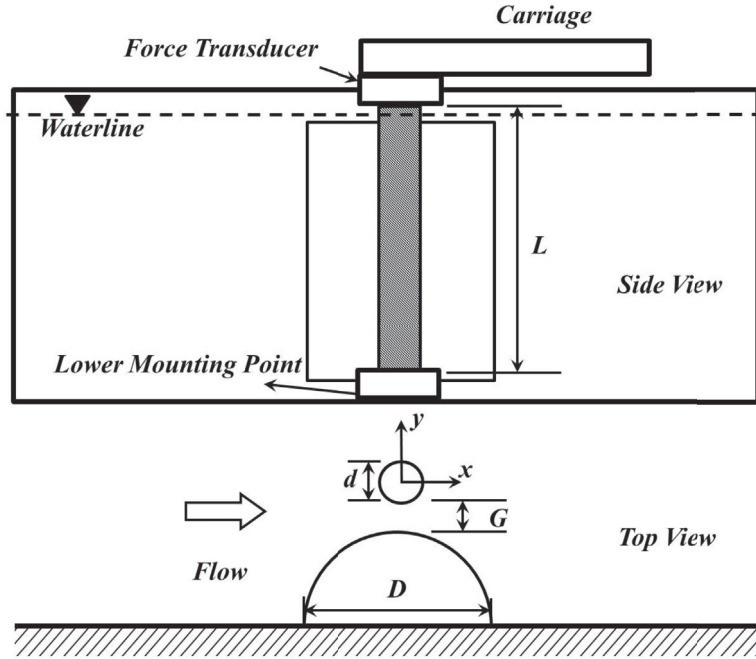
Fig. 1. Schematic diagram of experimental configuration.

Table 1
Model parameters.

Model parameters	Values
Large cylinder diameter D	2.54 cm
Model diameter d	0.953 cm
Model length L	58.1 cm
Model mass per unit length m_0	0.0983 kg/m
Model damping ratio ζ	0.082
Gap-to-diameter ratio G/d	1.0, 2.0, 3.0, 4.0, ∞

$G/d = \infty$ represents flexible model in the open flow.

measurement for flexible cylinder VIV experiments, the optical tracking system provides both temporally and spatially dense direct measurement on the model displacement, which helps to reveal more physical phenomena missed by traditional measurement tools [16]. One camera was installed over 80d downstream of the model to measure CF vibration while two cameras were installed 50d beside the model to measure IL vibration. At the same time, one 1500-lumen underwater light was installed to provide enough camera background lighting.

Corresponding image processing and motion tracking code have been developed to capture and follow the trajectory of either white or black markers [17]. The code follows the general protocol of the motion-based multiple object tracking method [18], and its key steps are shown in the flowchart of Fig. 2. In the first step of image processing, an appropriate color threshold is selected to convert color images into binary frames. Second, via blob analysis, the centroids and the bounding boxes of the objects will be detected in the current frame, and then the code calls for the track prediction/assignment function. In order to follow the object well instead of noise, based on the Euclidean distance between the assigned track location of the current frame and the Kalman filter predicted track location, it will decide whether to update the track position or delete the track as it is viewed as noise. In Fig. 3, we display a sample frame of the raw and tracked images for one of the cameras.

2.3. Data processing

2.3.1. Inverse vortex force

Due to the small bending stiffness, the current experiment can simply be modeled as a taut string subject to distributed external forces along the model, as in the following equation:

$$\mu \frac{\partial^2 u(x,t)}{\partial t^2} - T\frac{\partial^2 u(x,t)}{\partial x^2} + \beta \frac{\partial u(x,t)}{\partial t} = p(x,t) \tag{1}$$
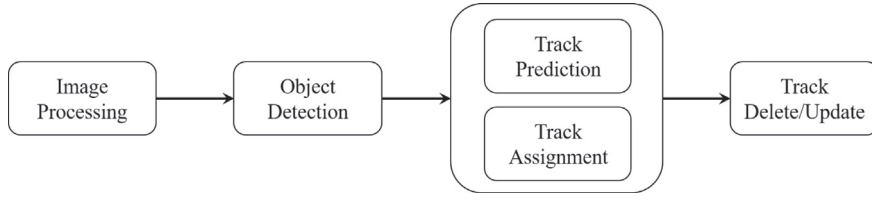
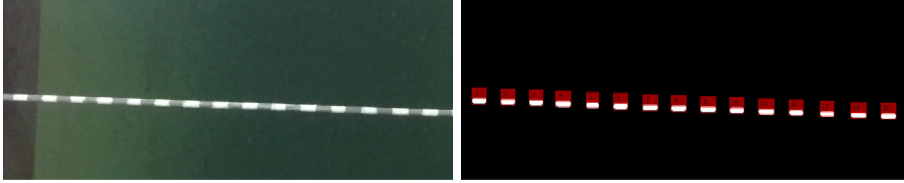**Fig. 2.** Flowchart of the imaging process and motion track method.

Fig. 3. Sample case of tracked motions: sample in the CF direction (left); processed image (right), and the red bounding box shows the ability to capture the motion of the white markers. (For interpretation of the references to color in this figure legend, the reader is referred to the Web version of this article.)

in which, μ is the structural mass per unit length of the model (without hydrodynamic added mass contribution), T is the model tension, β is the structural damping, $u(x,t)$ is the displacement for either the CF or the IL direction and $p(x,t)$ is the external hydrodynamic force per unit length on the model. With the dense temporal and spatial measurement of the model displacement in the CF and the IL directions, we can inversely calculate the vortex force $p_{i,j}$ exerted on the model node L_j at the time t_i, as follows,

$$p_{i,j} = \mu_j \frac{u_{i+1,j} + u_{i-1,j} - 2u_{i,j}}{\Delta t^2} - T_j \frac{u_{i,j+1} + u_{i,j-1} - 2u_{i,j}}{\Delta x^2} + \beta \frac{u_{i+1,j} - u_{i-1,j}}{2\Delta t} \tag{2}$$

Hence the mean and fluctuating non-dimensional hydrodynamic coefficient at different locations along the model will be as follows,

$$\overline{C}(j,t) = \frac{\frac{1}{n}\sum_{i=1}^{n} p_{i,j}}{0.5\rho U^2 d} \tag{3}$$

$$\widetilde{C}(j,t) = \frac{p_{i,j} - \frac{1}{n}\sum_{i=1}^{n} p_{i,j}}{0.5\rho U^2 d} \tag{4}$$

in which ρ is the fluid density and U is the towing speed for each experiment case.

We are then able to acquire the force coefficient in phase with velocity C_v, the force coefficient in phase with acceleration C_a, and the added mass coefficient C_m in either the CF or the IL direction at location j along the model as follows,

$$C_v(j) = \frac{\frac{2}{T_s}\int_{T_s}(\widetilde{C}(j,t)\dot{\widetilde{\xi}}(j,t))dt}{\sqrt{\frac{2}{T_s}\int_{T_s}(\dot{\widetilde{\xi}}^2(j,t))dt}} \tag{5}$$

$$C_a(j) = \frac{\frac{2}{T_s}\int_{T_s}(\widetilde{C}(j,t)\ddot{\widetilde{\xi}}(j,t))dt}{\sqrt{\frac{2}{T_s}\int_{T_s}(\ddot{\widetilde{\xi}}^2(j,t))dt}} \tag{6}$$

$$C_m(j) = -\frac{2U^2}{\pi d^2} \cdot \frac{\int_{T_s}(\widetilde{C}(j,t)\ddot{\widetilde{\xi}}(j,t))dt}{\int_{T_s}(\ddot{\widetilde{\xi}}^2(j,t))dt} \tag{7}$$

in which $\widetilde{\xi}$ is the CF and the IL displacement non-dimensionalized by the model diameter d, and $\dot{\widetilde{\xi}}$ and $\ddot{\widetilde{\xi}}$ are the first and second derivatives of ξ, namely the velocity and the acceleration at each location.

2.3.2. Instantaneous phase analysis

Another data analysis method used is to calculate the instantaneous phase angle between the CF and the IL vibrations along the model. Due to the different frequencies between the two signals, the phase cannot be obtained merely via Fourier analysis and calls for Hilbert Transformation, as follows.

Let $w(t)$ be a signal and $\mathbf{H}(w)$ be its Hilbert Transform. The Hilbert Transformation allows representing the instantaneous phase $\theta_w(t)$ and amplitude $A_w(t)$ of signal, in the form:

$$\mathbf{H}(w) = A_w(t)e^{i\theta_w(t)} \tag{8}$$

The instantaneous phase between two signals is then given by

$$\theta_{xy}(t) = -R_0\theta_{wy}^n(t) + \theta_{wx}^m(t) \tag{9}$$

in which θ_{xy} is the phase difference between the CF and the IL motions, m and n refer to the mode number in the CF and the IL directions and R_0 is the ratio of the dominant frequencies between the two signals. In the current research R_0 is chosen to be 2 and $m = 2n$.

3. Experimental results and discussion

Results of the experiment are presented in this section, and they are plotted mainly against the reduced velocity Ur, which is defined as follows,

$$Ur = \frac{U}{f_{n1}d} \tag{10}$$

in which, f_{n1} is the 1st natural frequency of a taut string in the water with a given tension. As the tension gets larger with the increasing velocity during different experimental runs, it affects the natural frequency of the system. Hence f_{n1} in this paper is calculated based on the measured tension in each experimental case, assuming a vibrating string in the water with uniform added mass coefficient $C_m = 1.0$ distributed along the model. Therefore, in the current experiment, the reduced velocity Ur ranges from 2.9 to 9.4.

3.1. Model frequency and displacement response

3.1.1. Mean displacement and steady force coefficient

Measured by the force transducer, the steady drag coefficients $\overline{C_d}$ of the smaller cylinder in the piggyback configuration for different gap-to-diameter ratios are plotted in Fig. 4 (left) against the reduced velocity Ur. For the flexible cylinder in the open flow, namely $G/d = \infty$, for each case, four repeated runs were performed, and the mean value is plotted with the purple round marker, while the maximum and minimum values are shown by the error bar. It is found that for $G/d = \infty$, $\overline{C_d}$ jumps from 1.1 at $Ur = 2.9$ when normally no large CF vibration may occur, to 1.57 at $Ur = 3.88$; and then varies mildly between 1.6 and 1.9 with the increasing reduced velocity, which is typical for VIV of the flexible cylinder, as the increase of the CF vibration amplitude will result in amplification for the steady drag coefficient $\overline{C_d}$ [19]. Such trends have also been observed for the cases of a flexible cylinder placed close to the half-buried large cylinder with different gap-to-diameter ratios. However, compared to the open flow case, there is a 50% $\overline{C_d}$ increase for the flexible cylinder close to the larger cylinder at G/d of 1.0, 2.0 and 3.0. For the case of $G/d = 4.0$, such amplification is smaller and hence $\overline{C_d}$ is getting close to that of the flexible cylinder in the open flow, as naturally the effect of the larger half buried cylinder will become much weaker when the flexible cylinder is farther away. When the flow passes the half cylinder on the plane, flow velocity may increase in a certain region above the cylinder
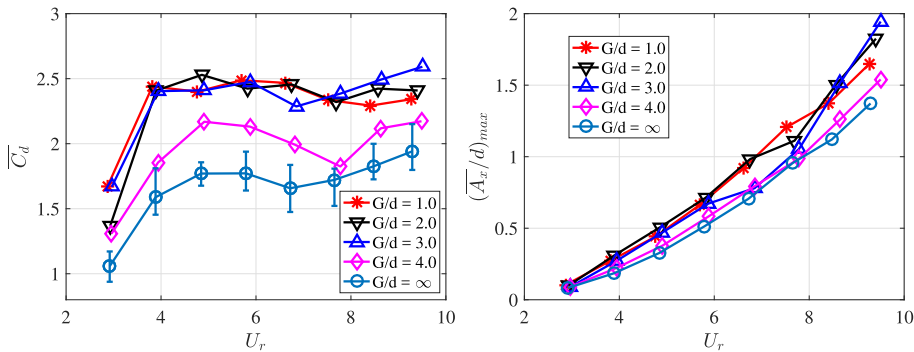

Fig. 4. Left: mean drag coefficient C_d for the different gap-to-diameter ratios against the reduced velocity Ur; right: maximum average IL displacement $(\overline{A_x}/d)_{\max}$ for the different gap-to-diameter ratios against the reduced velocity Ur.
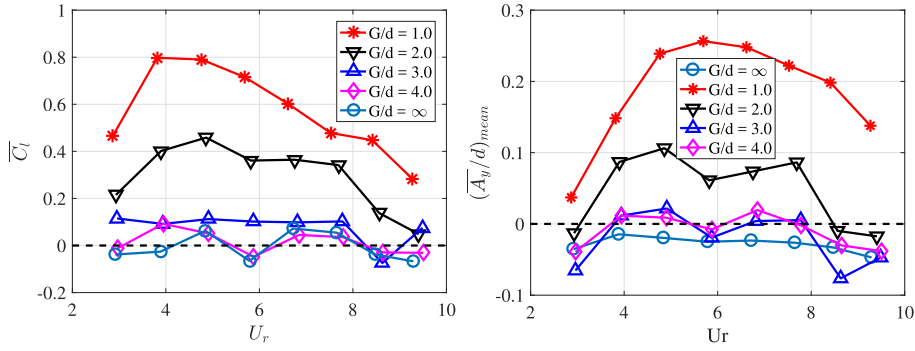
Fig. 5. Left: mean lift coefficient C_l for the different gap-to-diameter ratios against the reduced velocity Ur; right: spatially average mean CF displacement $(\overline{A_y}/d)_{mean}$ for the different gap-to-diameter ratios against the reduced velocity Ur.

[20]. For the smaller gap-to-diameter ratio case, the smaller cylinder gets closer to the large diameter cylinder and enters into the high-velocity region, and therefore it increases the drag force. If we use the incoming uniform velocity for non-dimensional coefficient calculation, we will see a rise of the drag coefficient.

The increase of the total drag force will increase the mean IL displacement and hence a larger axial tension. In Fig. 4 (right), we plot the maximum of the mean IL displacement along the flexible model for different gap-to-diameter ratios against the reduced velocity Ur. Due to the drag amplification for the cases of G/d from 1.0 to 3.0, it can be seen that for the same Ur flexible cylinder with G/d from 1.0 to 3.0 will have a more significant mean IL displacement, compared to the case of open flow as well as $G/d = 4.0$.

The steady lift coefficient is also a critical consideration for the smaller cylinder in the piggyback configuration, as the smaller cylinder may be pushed away from or pulled close to the larger cylinder, result in a non-zero mean CF displacement. If the steady lift force for the smaller cylinder points towards the larger cylinder, it will cause a decrease of the gap, and hence it will increase the possibility of the crash between the two cylinders. The mean lift coefficient $\overline{C_l}$ is plotted in Fig. 5 (left) for all the cases against the reduced velocity Ur, and the total spatial average mean CF displacement $(\overline{A_y}/d)_{mean}$ is plotted in Fig. 5 (right). Fig. 5 (left) shows that when the small cylinder is far away from the large cylinder (gap-to-diameter ratio larger than 2.0), the mean lift coefficient is close to zero, and therefore in Fig. 5 (right), small flexible cylinder vibrates around zero mean CF displacement $(\overline{A_y}/d)_{mean}$ for all U_r. However, shown in Fig. 5 (left), for the case of $G/d = 1.0$ and $G/d = 2.0$, there is a positive steady lift force applied on the flexible model that points away from the larger half-buried cylinder on average. Therefore, in Fig. 5 (right), it shows the smaller cylinder is pushed away from the larger cylinder and hence vibrates around a positive mean CF displacement $(\overline{A_y}/d)_{mean}$. And such a steady lift force is stronger for smaller $G/d = 1.0$, compared to $G/d = 2.0$. A similar comparison can be found in Williamson's work [21] on the fluid force on the small cylinder one diameter away from a cylinder with a 2.5 times larger diameter oscillating in the still water at $KC = 2\pi\frac{A}{D} = 28$. Similarly a large steady lift force was found on the small cylinder pointing away from the larger cylinder.
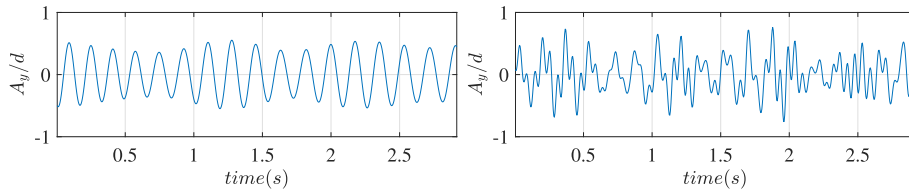

Fig. 6. Sample trace of CF displacement: $G/d = \infty$, $Ur = 6.72$ (left); $G/d = 1.0$, $Ur = 6.61$ at $L/d = -48$ (right).
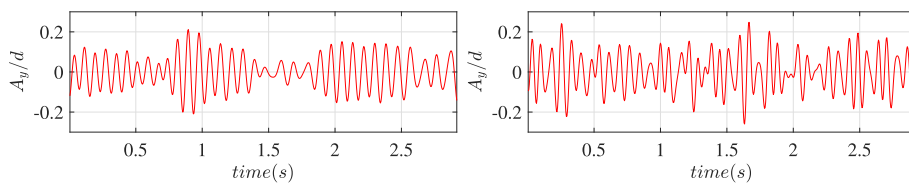

Fig. 7. Sample trace of IL displacement for $G/d = \infty$, $Ur = 6.72$ (left); $G/d = 1.0$, $Ur = 6.61$ at $L/d = -48$ (right).

3.1.2. Modal frequency and displacement response

Sample traces of the CF and the IL displacements for $G/d = \infty$, $Ur = 6.72$ and $G/d = 1.0$, $Ur = 6.61$ at $L/d = -48$ are picked and plotted in Fig. 6 and Fig. 7. It can be seen that for $G/d = \infty$, small flexible cylinder vibrates at a relatively mono-frequency and therefore time trace of the CF displacement at $L/d = -48$ is regular. However, in Fig. 6 (right) of $G/d = 1.0$, time trace of the CF displacement at $L/d = -48$ is rather chaotic and different frequency components coexist at the same time. A similar phenomenon can also be observed for the IL oscillation for different gap-to-diameter ratios in Fig. 7. The corresponding CF and the IL displacement FFT results for all 5 experimental setups of Ur around 6.6 at location $L/d = -48$ are plotted in Fig. 8 (a) to (j). The result from Fig. 8 (i) and (j) shows a typical VIV frequency response of a uniform flexible cylinder facing a uniform current that there is a sharp narrow-band mono-frequency response (1st *harmonic*) in the CF direction at 6.28 Hz, and a small yet detectable 3rd harmonic term can also be found. Meanwhile, in the IL direction, after filtering out the mean displacement, a sharp mono-frequency of 2nd harmonic response is observed. On the contrary, from Fig. 8 (a) to (h), it displays the frequency response for four different gap-to-diameter ratios from 1.0 to 4.0. It is observed that instead of the narrow-band response in the CF and the IL directions, the frequency response of the smaller flexible cylinder is wider in both directions, especially for the case of $G/d = 1.0$. Furthermore, for the case of gap-to-diameter ratio of 1.0, an exceptionally strong 3rd harmonic motion can be found, reaching almost 40% of the 1st harmonic motion in the CF direction, and with the increase of the gap-to-diameter
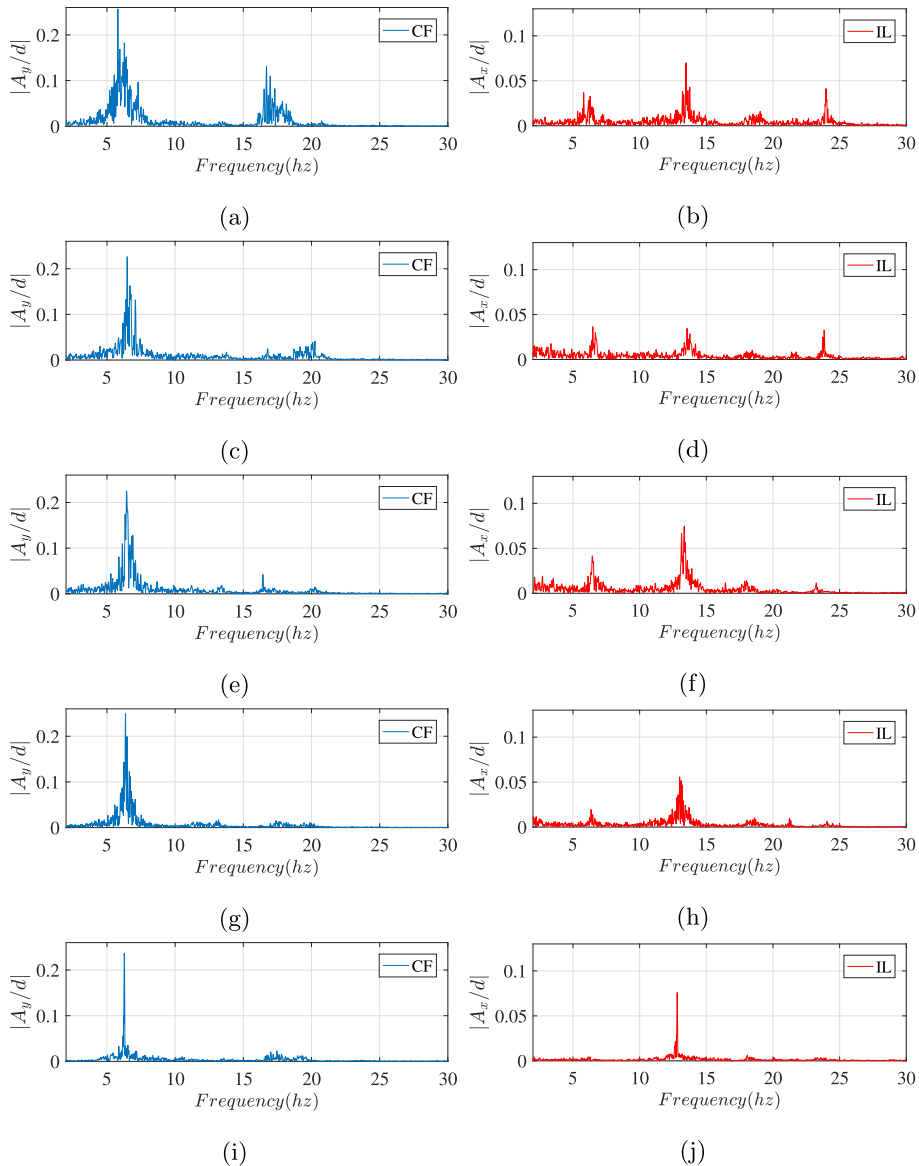

Fig. 8. CF (left) and IL (right) FFT result at $L/d = -48$ for different gap-to-diameter ratios: (a) and (b): $G/d = 1.0$, $Ur = 6.61$; (c) and (d): $G/d = 2.0$, $Ur = 6.75$; (e) and (f): $G/d = 3.0$, $Ur = 6.81$; (g) and (h): $G/d = 4.0$, $Ur = 6.81$; (i) and (j): $G/d = \infty$, $Ur = 6.72$.
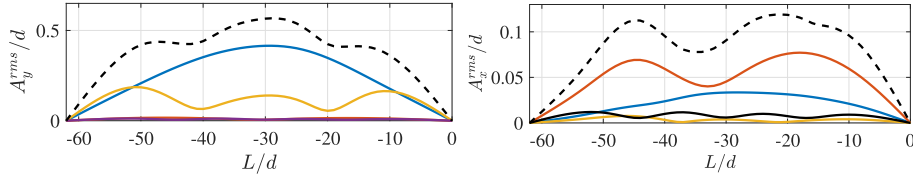
Fig. 9. Total (black dash line) and first 4 harmonics (1st: blue; 2nd: red; 3rd: yellow; 4th: black solid line) of CF (left) and IL (right) displacement RMS for $G/d = 1.0$, $Ur = 6.61$. (For interpretation of the references to color in this figure legend, the reader is referred to the Web version of this article.)
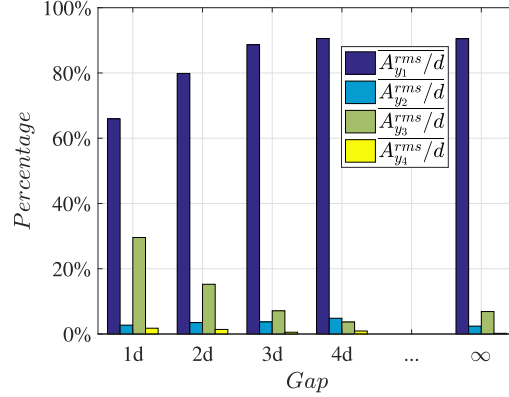

Fig. 10. Percentage of spatial average CF displacement RMS of first 4 harmonic for the different gap-to-diameter ratios at Ur around 6.6.

ratio, such large 3rd harmonic motion starts to disappear. Meanwhile, in the IL direction, although we can still find the 2nd harmonic motion, there are multiple different frequency harmonics (1st, 2nd, 3rd and 4th harmonics can be all observed in the IL direction.) found for the flexible cylinder close to the half-buried larger cylinder. We find that even for the case of gap-to-diameter ratio reaching 3.0, a very strong 1st harmonic motion coexist in the IL direction at the same time. In addition, when the gap-to-diameter ratio decreases to 1.0 and 2.0, a clear 4th harmonic and a detectable 3rd harmonic motion can be observed in the IL direction as well.

In order to better reveal such phenomena, the CF and the IL displacement RMS along the model is calculated for the first four harmonic and total motion. In Fig. 9, it shows the CF and the IL displacement RMS result for $G/d = 1.0$, $Ur = 6.61$. It can be seen in Fig. 9 (left) that the separated 1st and 3rd frequency harmonic induced motion in the CF direction can be found comparable with each other and contribute to the total CF displacement. Meanwhile, Fig. 9 (right) reveals that in the IL direction, all 1st to 4th frequency harmonic induced motion can be observed and contribute to the total IL displacement. The percentage of their spatial average is defined and calculated based on the following equation,

$$Percentage = \frac{\overline{A^{rms}_{(x/y)_n}}}{\overline{A^{rms}_{(x/y)_1}} + \overline{A^{rms}_{(x/y)_2}} + \overline{A^{rms}_{(x/y)_3}} + \overline{A^{rms}_{(x/y)_4}}} \tag{11}$$
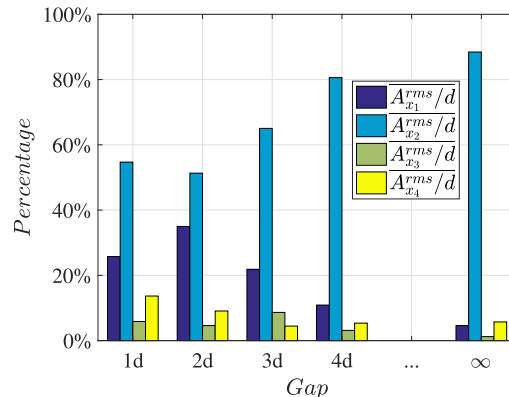

Fig. 11. Percentage of spatial average IL displacement RMS of first 4 harmonic for the different gap-to-diameter ratios at Ur around 6.6.
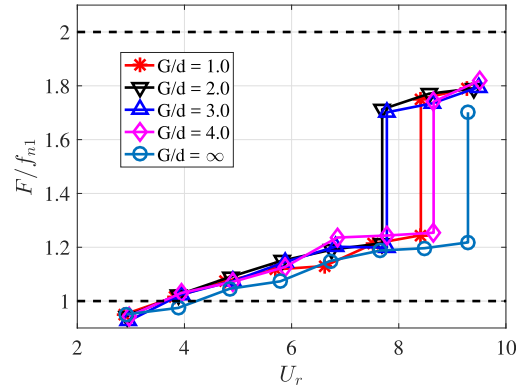
Fig. 12. The non-dimensional frequency F/f_{n1} for the different gap-to-diameter ratios against the reduced velocity Ur.

The CF results of Ur around 6.6 for all G/d are displayed in Fig. 10. It reveals that with the decrease of the gap-to-diameter ratio between the smaller and bigger cylinder, in the CF direction, the spatial average of the 3rd harmonic motion RMS will increase and it reaches over 30% for $G/d = 1.0$. Meanwhile, the IL results of Fig. 11 show that at smaller gap-to-diameter ratios, 1st and 4th harmonic motion are of the same order of the 2nd harmonic term. When $G/d = 4.0$, the results start to resemble the open flow case in both directions. These phenomena have not been observed before and require further attention as a large 3rd harmonic motion induced by the existence of the half-buried cylinder will result in a significant decrease in the fatigue life of the pipeline. In addition, the mechanism behind the enhancement of the 3rd harmonic in the CF direction and the coexistence of the multiple harmonics in the IL direction calls for future studies including flow visualization and rigid model experiment similar to the one by Chen et al. that when a smooth cylinder was forced to oscillate close to a plate in the CF direction, a strong 1st harmonic in the IL direction was observed [22].

Picking out the 1st harmonic frequency from the FFT analysis, the non-dimensional frequency F/f_{n_1} against the reduced velocity Ur is hence plotted in Fig. 12. As for the open flow case, F/f_{n_1} keeps close to 1 for Ur smaller than 9 and then jump close to 2, indicating a modal switch from 1st to 2nd in the CF direction. This non-dimensional frequency jump is also observed for all the other experimental cases of different gap-to-diameter ratios. However, a difference can be found that such jump occurred at a smaller reduced velocity Ur for gap-to-diameter ratios of 1.0–3.0.

The maximum of the CF and the IL total displacement RMS A_y^{rms}/d and A_x^{rms}/d along the model for different experimental cases are plotted in Fig. 13 and Fig. 14. In the CF direction, the result shows a similar trend for all the different gap-to-diameter ratios that $(A_y^{rms}/d)_{max}$ will first increase with the increasing reduced velocity but experience a sudden drop between the modal switch. However, due to the existence of the large 3rd harmonic motion, for $G/d = 1.0$, $(A_y^{rms}/d)_{max}$ is larger for the rest of the cases, reaching maximum RMS of 0.63d. Such amplification of the total motion need to take into great consideration, as such larger motion may increase the possibility of the two cylinders crushing with each other. In addition, compared to the open flow case, the maximum of the total IL displacement RMS does not vary too much among all the cases, and in the current experiment, the IL displacement RMS is found to be of 15–20% of that in the CF direction.
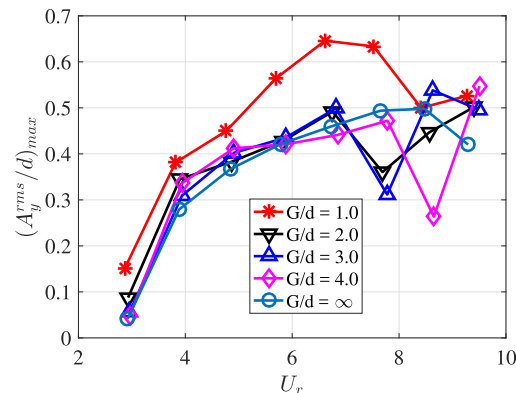

Fig. 13. The maximum CF displacement RMS $(A_y^{rms}/d)_{max}$ along the model for the different gap-to-diameter ratios against the reduced velocity Ur.
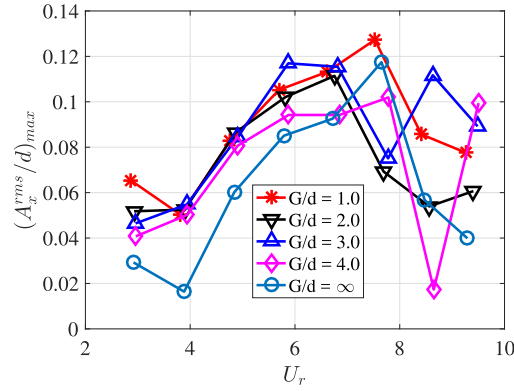
Fig. 14. The maximum IL displacement RMS $(A_x^{rms}/d)_{max}$ along the model for the different gap-to-diameter ratios against the reduced velocity Ur.
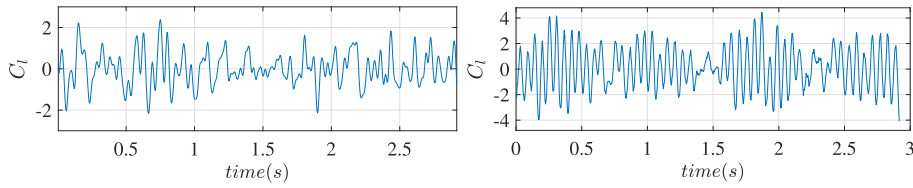

Fig. 15. Sample trace of the lift coefficient for $G/d = \infty$, $Ur = 6.72$ (left) and $G/d = 1.0$, $Ur = 6.61$ (right) at $L/d = -48$.

3.2. Inverse vortex force

Hydrodynamic forces along the model were reconstructed based on the equation (2), and it is plotted in Fig. 15 the lift coefficient at $L/d = -48$ for $G/d = \infty$ and $G/d = 1.0$ around $Ur = 6.6$. It is found that the maximum amplitude and the major frequency of C_l for $G/d = 1.0$ is higher than that of $G/d = \infty$ due to the existence of the higher harmonic force associated with the strong 3rd harmonic motion. In Fig. 16, it is plotted the separated 1st and 3rd harmonic lift coefficient RMS along the model for $G/d = \infty$ and $G/d = 1.0$ around $Ur = 6.6$. It is found that spatially 1st and 3rd harmonic lift coefficient for both $G/d = \infty$ and $G/d = 1.0$ have one and three half wavelength separately. Furthermore we find that for $G/d = \infty$, the amplitude of the 3rd harmonic force is around 4–5 times smaller that of the 1st harmonic force, which is similar to the former much larger scale experiment observations [23]. On the contrary, in the case of $G/d = 1.0$, we find that the amplitude of the 3rd harmonic force greatly amplified and it is even bigger than that of the 1st harmonic force. Same as the definition as in the equation (11) for the amplitude, we calculated the percentage of the spatial average for the first four harmonics of the drag and the lift coefficient RMS ($C_{d_n}^{rms}$ and $C_{l_n}^{rms}$) based on the following equation,

$$Percentage = \frac{\overline{C_{(l/d)_n}^{rms}}}{\overline{C_{(l/d)_1}^{rms}} + \overline{C_{(l/d)_2}^{rms}} + \overline{C_{(l/d)_3}^{rms}} + \overline{C_{(l/d)_4}^{rms}}} \tag{12}$$

Results are shown in Fig. 17 for the percentage of the spatial average of the first four harmonic lift coefficient RMS against the reduced velocity for all gap-to-diameter ratios. We find that for the smallest gap-to-diameter ratio case of $G/d = 1.0$ in the current experiment, spatial average of the 3rd harmonic lift coefficient RMS can reach more than 50% of the total lift coefficient. Such a phenomenon is consistent over the entire reduced velocity performed in the current research. It is observed that the strength of the 3rd harmonics decreases with the increase of the gap and the percentage of the first four harmonic force
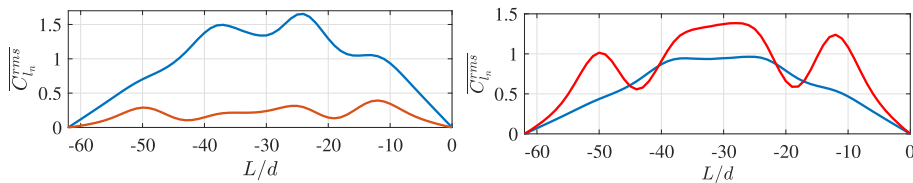

Fig. 16. 1st farmonic (blue) and 3rd harmonic (red) lift coefficient RMS along the model for $G/d = \infty$, $Ur = 6.72$ (left) and $G/d = 1.0$, $Ur = 6.61$ (right). (For interpretation of the references to color in this figure legend, the reader is referred to the Web version of this article.)
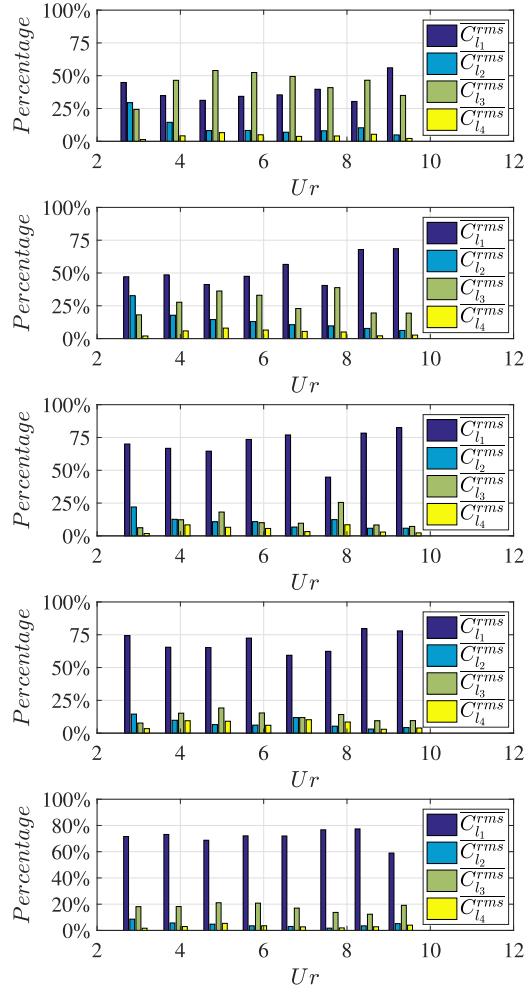
Fig. 17. Percentage of first 4 harmonic spatial average lift coefficient RMS ($\overline{C_{l_n}^{rms}}$) against the reduced velocity Ur (from top to bottom: $G/d = 1.0$, $G/d = 2.0$, $G/d = 3.0$, $G/d = 4.0$ and $G/d = \infty$).

coefficient resembles between the case of open flow and $G/d = 4.0$. Meanwhile, we plot in Fig. 18 the percentage of the spatial average of the first four harmonic drag coefficient RMS against the reduced velocity for all gap-to-diameter ratios. As expected, for the small gap-to-diameter ratio case of $G/d = 1.0$, 2nd harmonic drag coefficient is no longer the dominating one as it accompanies with a substantial contribution from the 1st and 4th harmonic terms.

3.3. Energy transfer and phase analysis between the CF and the IL vibration

The lift coefficient in phase with velocity C_{lv} is an important factor for VIV in the CF direction, as it determines whether the energy will be transfer from the fluid to structure or be damped out from structure to fluid. When C_{lv} is larger than zero, it indicts positive net energy from fluid to structure and hence the vibration amplitude may increase [24]. Furthermore, Dahl [25] and Bourguet [26] experimentally and numerically found that for both rigid and flexible cylinder VIV, positive C_{lv} was largely associated with the counter-clockwise trajectory between the CF and the IL vibrations. Hence, in Figs. 19–21, we plot the phase angle between 1st harmonic motion in the CF direction and 2nd harmonic motion in the IL direction, as well as the corresponding C_{lv} along the cylinder inversely calculated from the model vibration for three different gap-to-diameter ratios. Though the C_{lv} magnitude and distribution may vary between different gap-to-diameter ratios at different reduced velocities, a clear correlation can be found between the phase angle θ_{xy} and the sign of the C_{lv}. Therefore, in Fig. 22, we plot the histogram of θ_{xy} corresponding to the positive C_{lv} region for different G/d cases. The result clearly shows that a positive C_{lv} region is strongly correlated to the counter-clockwise trajectory between the CF and the IL vibrations ($0° < \theta_{xy} < 180°$). Such a principle still holds for the flexible model close to the half-buried larger cylinder with different gap-to-diameter ratios.
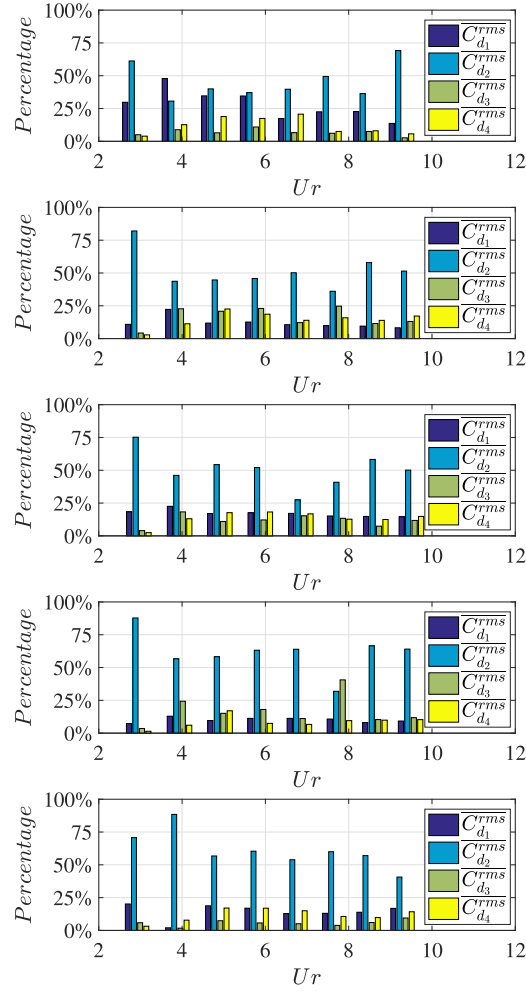
Fig. 18. Percentage of first 4 harmonic spatial average drag coefficient RMS ($\overline{C_{d_n}^{rms}}$) against the reduced velocity Ur (from top to bottom: $G/d = 1.0, G/d = 2.0, G/d = 3.0$, $G/d = 4.0$ and $G/d = \infty$).
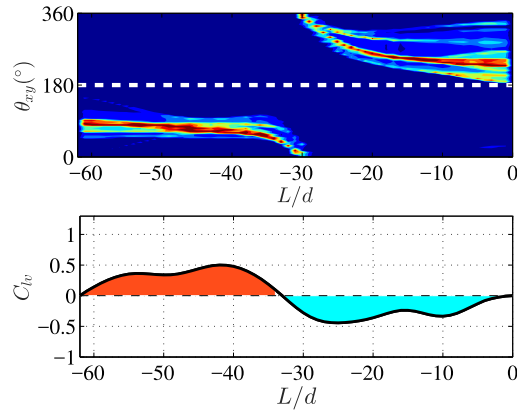

Fig. 19. $G/d = \infty, Ur = 6.72$: phase angle θ_{xy} (top) between CF 1st harmonic motion and IL 2nd harmonic motion; lift coefficient in phase with velocity C_{lv} (bottom) along the model.

Fig. 20. $G/d = 1.0$, $Ur = 4.76$: phase angle θ_{xy} (top) between CF 1st harmonic motion and IL 2nd harmonic motion; lift coefficient in phase with velocity C_{lv} (bottom) along the model.

Fig. 21. $G/d = 2.0$, $Ur = 7.69$: phase angle θ_{xy} (top) between CF 1st harmonic motion and IL 2nd harmonic motion; lift coefficient in phase with velocity C_{lv} (bottom) along the model.
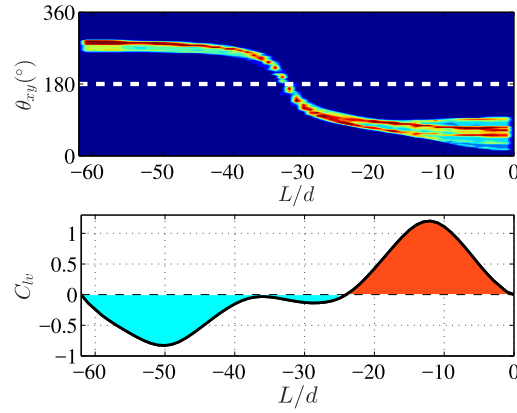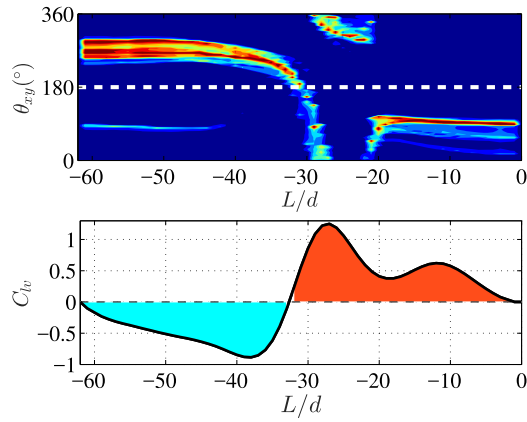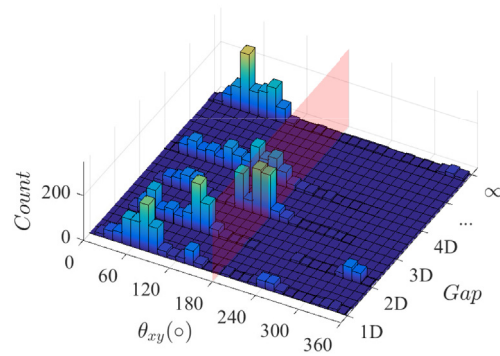

Fig. 22. Histogram of phase angle θ_{xy} between the CF and the IL vibrations for positive lift coefficient in phase with velocity C_{lv} along the model.

4. Conclusion

We experimentally investigated the flexible cylinder VIV of the small cylinder in a piggyback configuration with the main pipeline half buried in the seabed. The effect of the gap-to-diameter ratio has been studied for five different cases including an open flow one ($G/d = \infty$) under the different reduced velocities. The conclusions are drawn as follows,

1. The existence of the larger half-buried pipe will increase the mean drag coefficient for the smaller flexible cylinder in the piggyback configuration when the gap-to-diameter ratio is small, as the interaction between two is stronger. This results in a larger mean IL displacement at the same reduced velocity for the small gap-to-diameter ratio case. Meanwhile, positive mean lift coefficient is found for the vibrating flexible cylinder pushing it away from the larger one, resulting in a positive mean CF displacement.

2. Compared to the narrow-band mono-frequency response in the CF (1st harmonic) and the IL direction (2nd harmonic) for the open flow case, smaller flexible cylinder closer to the larger half buried cylinder displays a wider-band response when the gap-to-diameter ratio is small. Meanwhile, there appears a strong 3rd harmonic motion in the CF direction for $G/d = 1.0$, while, in the IL direction, frequency response is much richer, including additional strong 1st and 4th and detectable 3rd harmonic motion, apart from the large 2nd harmonic motion.

3. For the smallest gap-to-diameter ratio case of $G/d = 1.0$ in the current experiment, the CF displacement RMS is enhanced due to the existence of the strong 3rd harmonic motion, while the IL displacement RMS is close among all the different gap-to-diameter ratios.

4. Compared to the open flow case, very strong 3rd harmonic lift force is found based on the reconstructed vortex force along the entire model. For $G/d = 1.0$ case, at some reduced velocities, spatial average of the 3rd harmonic lift force may reach more than 50% of the total lift force, namely larger than that of the 1st harmonic lift force. The strength of the 3rd harmonic lift force will decrease with the increase of the gap-to-diameter ratio.

5. Similar to the open flow case that the positive C_{lv} region of the flexible model will be dominated by θ_{xy} from 0° to 180°, namely the counter-clockwise trajectory between the CF and the IL motions, such principle still holds for the smaller flexible cylinder in the piggyback configuration with main pipeline half buried int the seabed.

Appendix A. Supplementary data

Supplementary data to this article can be found online at https://doi.org/10.1016/j.jsv.2019.02.038.

References

[1] T. Sarpkaya, A critical review of the intrinsic nature of vortex-induced vibrations, J. Fluids Struct. 19 (4) (2004) 389–447.
[2] H. Mukundan, Y. Modarres-Sadeghi, J.M. Dahl, F.S. Hover, M.S. Triantafyllou, Monitoring viv fatigue damage on marine risers, J. Fluids Struct. 25 (4) (2009) 617–628.
[3] Y. Xu, S. Fu, Y. Chen, Q. Zhong, D. Fan, Experimental investigation on vortex induced forces of oscillating cylinder at high Reynolds number, Ocean Syst. Eng. 3 (3) (2013) 167–180.
[4] P.W. Bearman, Vortex shedding from oscillating bluff bodies, Annu. Rev. Fluid Mech. 16 (1) (1984) 195–222.
[5] P. Bearman, A. Wadcock, The interaction between a pair of circular cylinders normal to a stream, J. Fluid Mech. 61 (3) (1973) 499–511.
[6] P. Bearman, M. Zdravkovich, Flow around a circular cylinder near a plane boundary, J. Fluid Mech. 89 (1) (1978) 33–47.
[7] Y. Zhou, Z. Wang, R. So, S. Xu, W. Jin, Free vibrations of two side-by-side cylinders in a cross-flow, J. Fluid Mech. 443 (2001) 197–229.
[8] C. Lei, L. Cheng, K. Kavanagh, Re-examination of the effect of a plane boundary on force and vortex shedding of a circular cylinder, J. Wind Eng. Ind. Aerod. 80 (3) (1999) 263–286.
[9] S. Kalghatgi, P. Sayer, Hydrodynamic forces on piggyback pipeline configurations, J. Waterw. Port, Coast. Ocean Eng. 123 (1) (1997) 16–22.
[10] Z.-P. Zang, F.-P. Gao, Steady current induced vibration of near-bed piggyback pipelines: configuration effects on viv suppression, Appl. Ocean Res. 46 (2014) 62–69.
[11] Z. Zang, F. Gao, J. Cui, et al., Vortex shedding and vortex-induced vibration of piggyback pipelines in steady currents, in: The Twenty-second International Offshore and Polar Engineering Conference, International Society of Offshore and Polar Engineers, 2012.
[12] Z.-P. Zang, F.-P. Gao, J.-S. Cui, Physical modeling and swirling strength analysis of vortex shedding from near-bed piggyback pipelines, Appl. Ocean Res. 40 (2013) 50–59.
[13] M. Zhao, L. Cheng, B. Teng, Numerical modeling of flow and hydrodynamic forces around a piggyback pipeline near the seabed, J. Waterw. Port, Coast. Ocean Eng. 133 (4) (2007) 286–295.
[14] M. Zhao, Influence of the position angle of the small pipeline on vortex shedding flow around a sub-sea piggyback pipeline, Coast Eng. J. 54 (03) (2012) 1250017.
[15] X. Wu, F. Ge, Y. Hong, A review of recent studies on vortex-induced vibrations of long slender cylinders, J. Fluids Struct. 28 (2012) 292–308.
[16] D. Fan, H. Du, M. Triantafyllou, Optical tracking measurement on vortex induced vibration of flexible riser with short-length buoyance module, in: APS Division of Fluid Dynamics Meeting Abstracts, 2016.
[17] D. Fan, M.S. Triantafyllou, et al., Vortex induced vibration of riser with low span to diameter ratio buoyancy modules, in: The 27th International Ocean and Polar Engineering Conference, International Society of Offshore and Polar Engineers, 2017.
[18] T.B. Moeslund, E. Granum, A survey of computer vision-based human motion capture, Comput. Vis. Image Understand. 81 (3) (2001) 231–268.
[19] J. Chaplin, P. Bearman, F.H. Huarte, R. Pattenden, Laboratory measurements of vortex-induced vibrations of a vertical tension riser in a stepped current, J. Fluids Struct. 21 (1) (2005) 3–24.
[20] M.S. Akoz, Investigation of vortical flow characteristics around a partially buried circular cylinder, Ocean Eng. 52 (2012) 35–51.
[21] C. Williamson, Fluid forces on a small cylinder in the presence of a large cylinder in relative oscillatory flow, Appl. Ocean Res. 7 (3) (1985) 124–127.
[22] Y. Chen, S. Fu, Y. Xu, D. Fan, High order force components of a near-wall circular cylinder oscillating in transverse direction in a steady current, Ocean Eng. 74 (2013) 37–47.
[23] Y. Modarres-Sadeghi, F. Chasparis, M. Triantafyllou, M. Tognarelli, P. Beynet, Chaotic response is a generic feature of vortex-induced vibrations of flexible risers, J. Sound Vib. 330 (11) (2011) 2565–2579.
[24] R. Gopalkrishnan, Vortex-induced Forces on Oscillating Bluff Cylinders, Ph.D. thesis, Massachusetts Institute of Technology, 1993.
[25] J.J.M. Dahl, Vortex-induced Vibration of a Circular Cylinder with Combined In-Line and Cross-Flow Motion, Ph.D. thesis, Massachusetts Institute of Technology, 2008.
[26] R. Bourguet, Y. Modarres-Sadeghi, G.E. Karniadakis, M.S. Triantafyllou, Wake-body resonance of long flexible structures is dominated by counterclockwise orbits, Phys. Rev. Lett. 107 (13) (2011) 134502.